Scenario with Combined Density and Heating Control to Reduce the Impact of Bootstrap Current in Wendelstein 7-X

P. Sinha,* D. Böckenhoff, M. Endler, J. Geiger, H. Hölbe,
H. M. Smith, T. S. Pedersen, Y. Turkin, and W7-X Team
Max-Planck-Institut für Plasmaphysik,
Wendelsteinstraße 1, 17491 Greifswald, Germany

(Dated: September 10, 2019)

Abstract

Wendelstein 7-X is a low-shear stellarator with an island divertor, formed by natural magnetic islands at the plasma edge and ten modular divertor units for particle and energy exhaust. For the island divertor concept to work properly, the device is optimized for small internal currents. In particular, the bootstrap current is minimized. Previous studies predicted a thermal overload of the targets at a particular location, due to the slow evolution of the toroidal net current in the initial phase of certain otherwise desirable high-power discharges. The present numerical study explores the neoclassical predictions for the bootstrap current in more detail and demonstrates, as a proof of principle, that a path from low density and low heating power to high density and full heating power exists, on which the bootstrap current remains constant. This offers the possibility to reach the predetermined toroidal net current at low heating power, where no overload will occur in the transient phase.

I. INTRODUCTION

Wendelstein 7-X (W7-X) is a large stellarator with five field periods, operated at the Greifswald site of the Max-Planck-Institut für Plasmaphysik (IPP) [1, 2]. Its magnetic field configuration was optimized for good MHD equilibrium and stability properties, low neoclassical transport and small bootstrap current in the long-mean-free-path (lmfp) regime, and good fast particle confinement at high β values. It aims to show that stellarator research can provide a magnetic configuration suitable for a reactor. The superconducting coil system consists of 50 non-planar coils of 5 different coil types and 20 planar coils of 2 different coil types. The 5 non-planar coil types and 2 planar coil types form one half module of the magnet system, two such half modules in stellarator symmetry form one module, which is repeated along the torus, following the fivefold symmetry of the device. Independent control of the currents in each of the coil types allows for considerable flexibility in changing the magnetic configuration. The aim is to operate W7-X in quasi-steady-state discharges at fusion relevant plasma parameters with a duration of up to 30 min.

The main heating system for this operation mode is Electron Cyclotron Resonance Heating (ECRH) [3], with ten continuous wave (cw) gyrotrons providing up to 1 MW each at 140 GHz for operating at a resonance field of 2.5 T. At medium plasma densities, the ECRH is operated in X2-mode (cut-off density at $1.2 \times 10^{20}\,\mathrm{m}^{-3}$). For densities beyond the X2 cut-off, O2-mode heating is used up to densities of about $2 \times 10^{20}\,\mathrm{m}^{-3}$ (cut-off at $2.4 \times 10^{20}\,\mathrm{m}^{-3}$), which has already been successfully demonstrated in the first divertor operation phase of W7-X [4, section 4]. At even higher densities O-X-B mode conversion is envisaged, which was tested in the predecessor experiment Wendelstein 7-AS (W7-AS) [5, 6]. In addition to heating, electron cyclotron current drive (ECCD) can be achieved by an appropriate setting of the ECRH launching mirrors. Further heating systems are neutral beam injection (NBI) with about 5 MW in 10 s pulsed operation [7], which has gone into operation in 2018, and ion cyclotron resonance heating (ICRH) with 4 MW [8] foreseen for the next operational phase, to start in 2021.

In order that the HELIAS concept of W7-X [9] be viable for a fusion reactor [10], a solution for particle and energy exhaust has to be provided. For the low-shear configuration of W7-X, an island divertor concept was chosen [11], which was successfully tested in the predecessor experiment W7-AS [12]. For the island divertor, the edge magnetic field topology has a specific resonant structure in which magnetic islands formed by a naturally occurring low-order-rational value of the rotational transform ι at the boundary of the plasma generate a separatrix, which guides the particle and power fluxes from the main plasma to the divertor targets designed for high power loads [13]. The target plates are arranged in 10 divertor units of equal shape, corresponding to the fivefold toroidal symmetry and to the up-down flip symmetry (stellarator symmetry) of the device (see Fig. 1).

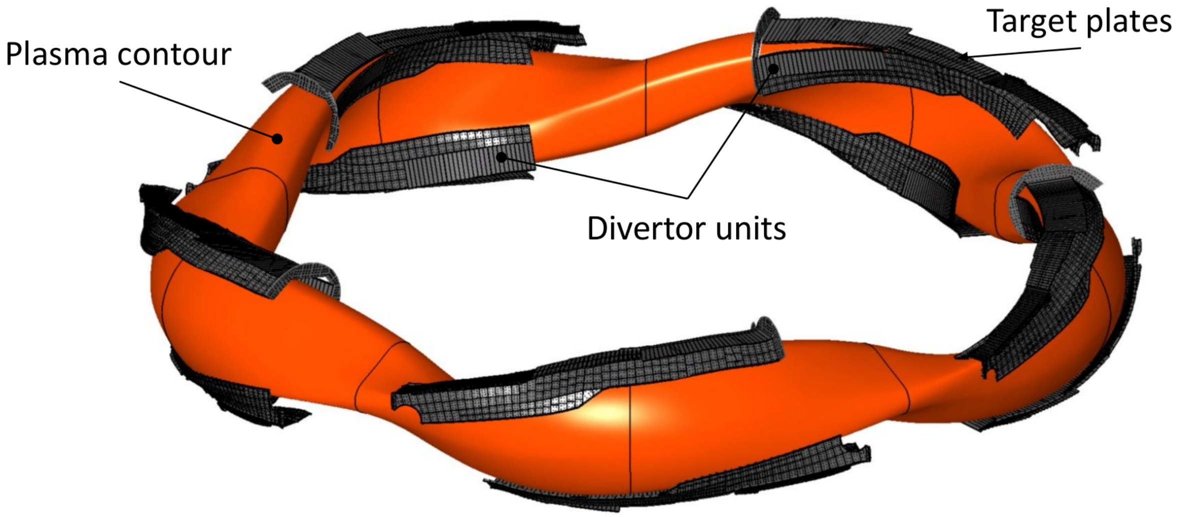

FIG. 1: Plasma column with the ten divertor units, positioned according to periodicity and stellarator symmetry [**?**].

The High Heat Flux (HHF) divertor units to be installed for future long-pulse operation are designed for stationary heat loads of $10\,\mathrm{MW/m^2}$ in the highest loaded areas [14]. However, due to technical restrictions, there are regions of the target plates where the allowable power density to the surface is significantly lower. A design view of one divertor unit is shown in Fig. 2.

The edge rotational transform is of extreme importance for the island divertor operation, as it determines the radial position of the magnetic islands. If there is a net toroidal current I_{tor}, it changes the rotational transform and thus displaces the island chain radially relative to the vacuum configuration. Because of the low shear, the variation of the toroidal current must therefore be limited to rather small values on the order of $10\,\mathrm{kA}$, or the impact on the magnetic configuration must be balanced by an appropriate adaptation of the field coil currents (or by ECCD [15]) (see section II).

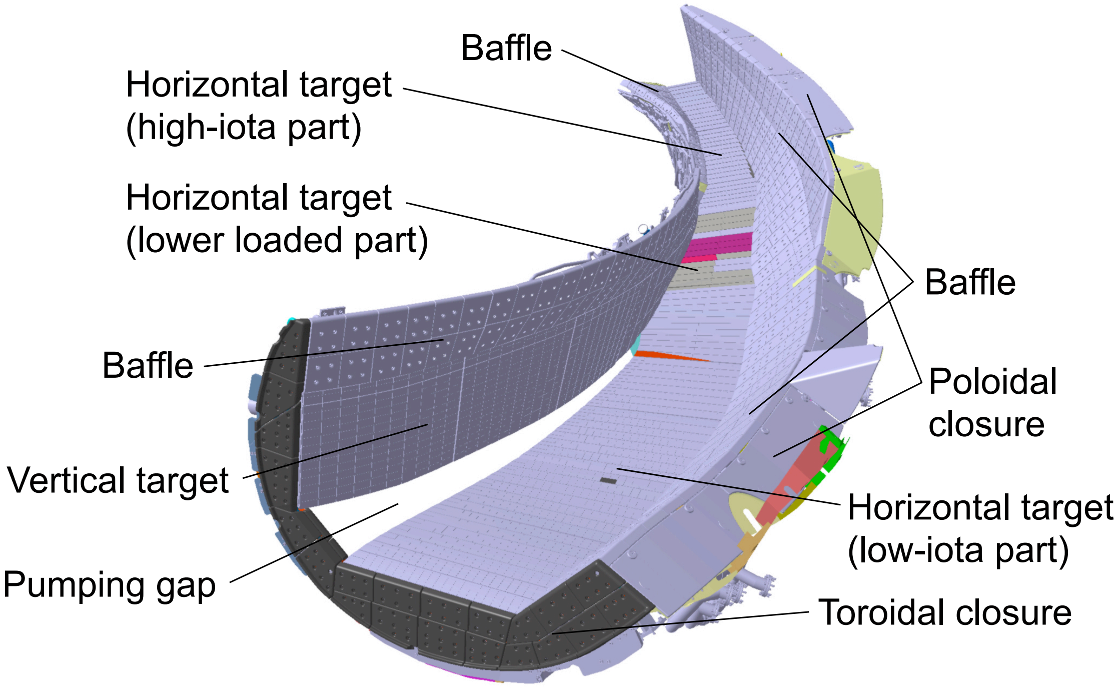
Baffle
Horizontal target
(high-iota part)
Horizontal target
(lower loaded part)
Baffle
Baffle
Poloidal
closure
Vertical target
Horizontal target
(low-iota part)
Pumping gap
Toroidal closure

FIG. 2: Lower divertor unit showing the different components.

Wendelstein 7-X is optimized for small bootstrap current I_{bs} [16]. However, in some scenarios, I_{bs}, as calculated from neoclassical theory, can still assume values on the order of 50 kA. The net toroidal current (consisting of the I_{bs} and an exponentially decaying shielding current which is induced by the self-inductance of the plasma) reaches steady state after several L/R times which, for W7-X plasma parameters, may require several tens of seconds:

$$I_{\mathrm{tor}} = I_{\mathrm{bs}}\,(1 - \exp(-t/\tau)), \tag{1}$$

where $\tau = L/R$ is the decay time constant of a current in a circular conductor with inductance L and resistance R (see [17] for a detailed discussion of the evolution of currents in a stellarator, including the role of bootstrap current and current drive). An example of the impact of the evolution of I_{tor} on the edge configuration is shown in Fig. 3.

The impact of the variation of the net toroidal current on the heat load pattern on the target plates can be significant and may have to be minimized. Specifically, the area of maximum heat load typically forms one or several narrow stripes with a width of a few centimeters in the poloidal direction and extending along the target in the toroidal direction. These stripes are called strike line(s), and their poloidal location on the targets is sensitive to I_{tor}. In particular, an attractive discharge scenario was identified [15] where, however,

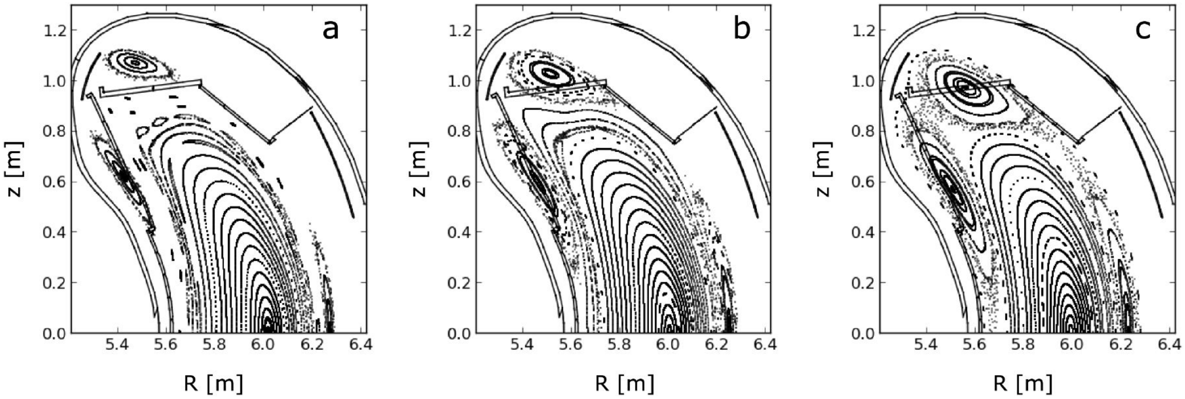

FIG. 3: Poincaré plot of different stages of evolution of the toroidal current in the "scraper element reference scenario" [15] (see section II): (a) 0 kA (b) 22 kA (transitional state) (c) 43 kA (final state) (from [18]).

the strike line would approach the pumping gap during the toroidal current equilibration, thus overloading the target edges bounding the pumping gap and possibly wall components behind the pumping gap (see Figs. 6 and 3) [19]. The analysis in [15], however, used neoclassical transport coefficients in the calculation of radial profiles, which had been calculated for a single density case in the magnetic "standard reference" configuration (which has similar vacuum field properties). The MHD equilibrium, neoclassical transport coefficients and radial profiles of plasma pressure and toroidal current density were therefore not consistent. Part of the present work is to calculate, in a proof-of-principle study, stationary plasma states with different values of I_{bs} and consistency between MHD equilibrium, neoclassical transport and radial profiles, which will be called "self-consistent solutions" in the following. The aim of this work is to demonstrate the existence of a sequence of such stationary states, where, first, a certain value of I_{bs} is achieved at low power and appropriate plasma density. During the evolution of this first plasma state from startup to the desired final stationary state, the configuration with significant power loads on sensitive locations of the targets will be passed at a low power level. The further plasma states of the sequence will then be chosen in such a way as to balance the scalings of I_{bs} with pressure gradient and with collisionality, such that I_{bs} is kept constant. The solution to this task is not entirely self-evident, since I_{bs} itself depends on MHD equilibrium (not only on the structure of $|B|$, but also on ι, i. e., the current density profile must be considered), plasma profiles (collisionality and radial electric field) and on the thermal transport calculated from the mono-energetic neoclassical transport coefficients in a subtle, non-linear way in a magnetic configuration like that of W7-X, which was optimized, among other criteria, for vanishing bootstrap current.

We note that we do not aim at describing a dynamic time evolution by solving time-dependent equations, but we investigate stationary states. For low power, where the overload is avoided, a slow evolution of the toroidal current can be tolerated, and for the phase with the final $I_{\rm bs}$, the toroidal current should be constant in this approach with no change of the location of the boundary islands. The detailed time evolution is therefore not considered here.

The paper is organized as follows. After revisiting the different solutions suggested to solve the overload problem and introducing our new approach in section II, we shall discuss the numerical method in section III. We shall then show a potential path from a low-density, low-power plasma to high-performance conditions without overloading the target edges at the pumping gap in section IV. After discussing these results and the underlying assumptions in section V, we summarize our conclusions in section VI.

II. SCHEMES TO MITIGATE THE IMPACT OF THE VARIATION OF THE TOROIDAL CURRENT

Different ways have been proposed to avoid the overloading of components during the evolution of the toroidal current density toward its steady-state profile. They can be grouped into two categories:

1. Transient modification of the magnetic configuration by external current drive or by changing the currents in the field coils,

2. modification of the plasma-facing components,

In this section, we shall first revisit the basic idea behind each of the schemes proposed so far and shortly discuss their respective disadvantages. We shall then introduce a third category, making use of the dependance of the bootstrap current on plasma density and temperature.

A. Current Drive

To keep the net value of I_{tor} in an acceptable range, Electron Cyclotron Current Drive (ECCD) can be applied [17]. The two major drawbacks of using this technique are, firstly, that it works efficiently only for intermediate or low plasma densities. Secondly, since the current is driven in a highly localized radial position, the rotational transform profile is strongly modified, giving rise to many low-order rational magnetic surfaces. While compensating the net current, ECCD therefore sacrifices the low-shear profile of the rotational transform, which may destabilize the plasma [15, 20, 21]. Experimentally, strong MHD activity has already been observed in discharges with ECCD [22].

B. Transient Change of Field Coil Currents

The most pronounced change in the plasma edge due to a net toroidal plasma current is the radial shift of the island chain in configurations with edge islands. This could also be compensated by adjusting the ratio of the planar and non-planar field coil currents. The edge rotational transform of the vacuum magnetic field would then be dynamically adjusted to compensate for the effect of the toroidal plasma current. First, a feed-forward scheme could be applied if the current evolution is known, as it was demonstrated on other stellarators (see, e. g., [23, 24]). There are, however, limits for the rate at which the currents in the superconducting field coils of W7-X can be changed. A first experiment with limited scope has been performed to test this option, the analysis of which is still ongoing. Ultimately, an ι control using the field coils would require a feedback system controlling the power supplies of the magnet system. This has not been planned originally. Technically, it would require considerable adjustments in the control and safety system of W7-X. We shall not discuss this method further here.

C. Addition of a Further Target Component

Another possibility to protect the edges of the pumping gap is the installation of a set of new actively cooled passive protection elements called Scraper Elements (SE) [19]. They prevent the heat flux from reaching the critical regions of the divertor, where it might overload the components during the transition to a stationary current state. However, numerical simulations indicate that the SEs could deteriorate the plasma performance since they significantly reduce the pumping efficiency [25]. This scheme has been tested in the first divertor operation phase with a set of only two SEs for 2 out of the 10 target units. Detailed analysis of the results is ongoing [26].

D. Controlling the Variation of Bootstrap Current by Control of Density and Heating Power

In the previous analysis of the overload problem, a final high-performance plasma state with a certain density and heating power was taken as the goal, and the resulting bootstrap current was calculated by a transport code (see section III). It was then assumed that density and heating power would quickly assume their target values, whereas the toroidal current would slowly evolve on the L/R time scale, overloading the target edges at the pumping gap during several tens of seconds.

However, the bootstrap current naturally depends not only on the magnetic configuration but also non-linearly on density and heating power. This offers the option to have for some desired magnetic configuration the same bootstrap current at low density and low heating power as at the high density, high heating power target state. The critical range of I_{tor} could then be reached and exceeded at reduced heating power levels, avoiding an overload. After that, a path with constant I_{bs} to high power and high density would be followed by a controlled increase of power and density. While ECRH power and its deposition profile is easily controlled, this is not as easy a task for plasma density and the density profile. Here, we shall nevertheless assume that these quantities can be sufficiently well controlled during a plasma discharge.

For the present proof-of-principle study, we choose a magnetic configuration which is as desirable as the one for which the scraper elements were conceived (SE reference configuration) [19, 27] but slightly different. The reason is that in this configuration, which has the same low neoclassical losses (see section IV C) and good MHD stability at a heating power of 10 MW as the standard reference configuration, I_{bs} is predicted to reach $\sim 30\,\mathrm{kA}$. Therefore the vacuum configuration is slightly adjusted to achieve divertor heat load patterns compatible with the technical limits of the water-cooled HHF divertor in the steady-state phase. As announced in secion I, we aim to develop a path consisting of stationary plasma scenarios, each of which has a consistent set of MHD equilibrium, neoclassical transport coefficients and plasma profiles from transport simulations, ranging from low power and low density to the desired high-density steady-state without overloading the divertor. The field coil currents for this new configuration are listed together with those of the SE reference configuration in Table I. In the following sections, we shall describe the computer codes and their assumptions and the resulting discharge path toward a high-performance plasma state.

TABLE I: Coil currents for the vacuum magnetic fields with 2.52 T on the magnetic axis at the ECR heating position for the configuration discussed in this paper ('new') and for the scraper element reference configuration [27] ('SE ref'). Here, I_1 to I_5 are the currents in the non-planar coils and I_A, I_B the ones in the planar coils. The offset in edge rotational transform of the 'new' vacuum field relative to the target configuration has been chosen to account for $I_{\text{tor}} = 30\,\text{kA}$.

[kA]	I_1	I_2	I_3	I_4	I_5	I_A	I_B
new	12.10	11.96	12.22	13.48	13.60	7.68	−4.06
SE ref	11.95	11.82	12.07	13.31	13.43	8.86	−2.86

III. MODELLING APPROACH

In this chapter, we discuss the building blocks of our analysis. In section III A, a general outline of their interrelation will be given. After that, we shall list the assumptions made in these numerical tools and indicate where more detailed descriptions can be found. We shall start with the three codes used to calculate self-consistent magnetic equilibrium configurations (in the sense defined in section I), the Variational Moments Equilibrium Code (VMEC) [28] and the EXTENDER code [29] (section III B), the Drift-Kinetic Equation Solver (DKES) [30] (section III C), and the Neoclassical Transport Simulation for Stellarators (NTSS) code [31] (section III D). We shall continue in section III E with a description how these codes have been used iteratively to obtain self-consistent radial profiles. We shall conclude this chapter by describing the calculation of thermal loads on the targets in a field line diffusion code [32] in section III F.

A. Interrelation of Numerical Tools

The radial profiles of toroidal current density and pressure for some W7-X configuration can be calculated by the NTSS transport code, which takes as input a radial density profile, a radial heating power profile, and coefficients describing neoclassical and anomalous transport. Neoclassical transport is important in stellarators in particular in the lmfp regime.

A table of (mono-energetic) neoclassical transport coefficients is obtained from the DKES code, which requires as input the magnetic equilibrium configuration (in terms of a Fourier representation of the magnetic flux surfaces and a radial profile of the rotational transform).

This description of the magnetic equilibrium configuration can be calculated by the VMEC code, which takes as input the vacuum magnetic field and the radial profiles of pressure and of toroidal current density.

Obviously, there exists a circular dependance between the output of these three codes and (at least part of) their input, as shown in Fig. 4. Until now, this iteration has not been automated, since the output of the codes (in particular of DKES) requires some assessment with regard to the accuracy of the results. In the past, the sequence of codes was iterated to a self-consistent solution (within the assumptions) for one scenario with very low bootstrap current (on the order of a few kA) and for a second scenario with ECCD to keep the toroidal net current equally small [21]. In this paper, we present for the first time self-consistent iteration results for configurations with larger bootstrap current. This has an impact on the iteration since the bootstrap current changes the ι profile which in itself influences the bootstrap current.

The iteration is started with assumed shapes for the radial profiles of pressure and toroidal current density (see section III E), together with an average β and a value of the toroidal net current.

Once the changes between iterations are negligible, the magnetic equilibrium configuration calculated by VMEC for the confinement region is used by the EXTENDER code to calculate the full magnetic field in the entire vacuum chamber, produced by the plasma in magnetohydrodynamic (MHD) equilibrium and by the external coils. This full field is then used to calculate the thermal load to the targets and other wall components in a field line diffusion code.

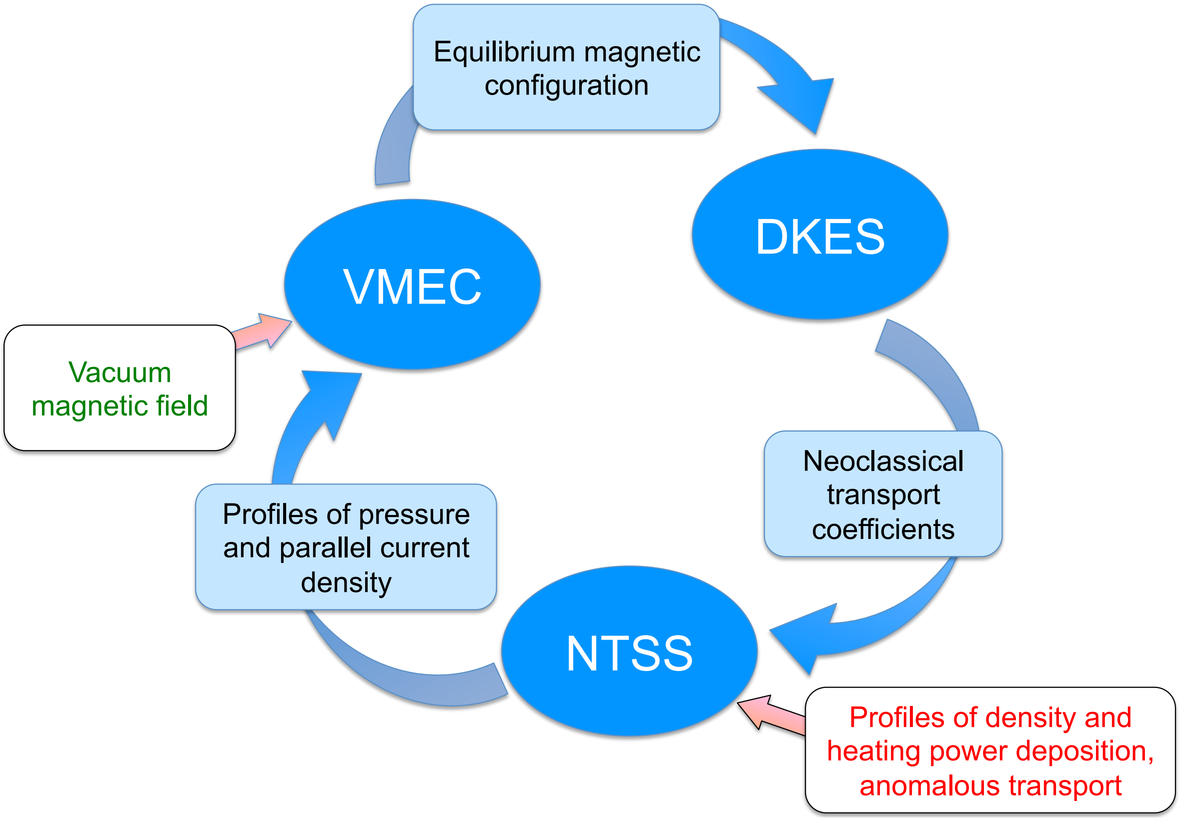
Equilibrium magnetic configuration
DKES
VMEC
Vacuum magnetic field
Neoclassical transport coefficients
Profiles of pressure and parallel current density
NTSS
Profiles of density and heating power deposition, anomalous transport

FIG. 4: Iterative modelling using the codes VMEC, DKES and NTSS to calculate a magnetic equilibrium configuration with consistent radial profiles and neoclassical transport coefficients.

B. VMEC and EXTENDER

VMEC is used to calculate the magnetic field in the presence of a plasma by solving the ideal MHD equations for a stationary equilibrium

$$\nabla \cdot \mathbf{B} = 0, \tag{2}$$

$$\mathbf{J} \times \mathbf{B} = \nabla p, \tag{3}$$

$$\nabla \times \mathbf{B} = \mu_0 \mathbf{J}. \tag{4}$$

VMEC assumes that the magnetic field forms nested flux surfaces, which are labeled by the value of the normalized toroidal flux s (VMEC's radial coordinate, running from 0 in the plasma center to 1 on the VMEC domain boundary). This surface limiting the computational domain is also assumed to be a flux surface. In a free-boundary calculation this defines the volume of the plasma. As basic input, VMEC requires the toroidal flux contained within this limiting surface. VMEC by itself has no way to determine whether these assumptions are valid or not and cannot judge on the size of its computational boundary. For our iterations aiming at a certain value of I_{bs} and hence at a fixed radial location of the bounding island chain, we used a fixed value of the toridal flux. Due to the assumption of nested flux surfaces, VMEC cannot treat islands or stochastic regions. However, the full field can be used to investigate the location of the boundary islands and of the separatrix to a leading order, and this information can be used to adjust the input parameters of VMEC accordingly to exclude the island region from the calculation domain, as described in [15]. In the sequence of calculations we kept the volume of the VMEC domain almost constant at $\sim 28\,\text{m}^3$. With this value, the 5/5 boundary islands are outside the VMEC domain for $I_{\text{tor}} = 30\,\text{kA}$. For simplicity, this volume was also used for the low-power, lower-density phase, where, with smaller toroidal currents, the boundary islands are further out, but where an overload of the critical divertor parts does not occur (see section IV C).

The model of nested flux surfaces is necessary for the iterative use with DKES and NTSS, which assume that transport is local and calculate the integral fluxes through (radial) and within (parallel) the flux surfaces.

Further basic input data to VMEC are the radial profiles of plasma pressure $p(s)$ and toroidal current density $j_{\text{tor}}(s)$.

To investigate the effects of the plasma currents on the edge islands and to study their impact on the interaction of the plasma with the divertor targets and the wall components, magnetic fields in the entire plasma vessel are required. For this purpose the EXTENDER code is employed which uses the virtual casing principle [33, 34] to calculate the fields outside of the VMEC domain generated by the plasma and combines them with the vacuum field to obtain the full field. For the field in the VMEC domain we do not use the VMEC field itself, but rather a combination of the VMEC field, the EXTENDER solution inside the VMEC domain and the vacuum field, which is calculated by Biot-Savart's law from the currents in the field coils, as described in [15]. The full field built in this way is well suited to investigate the edge region of the magnetic configuration and its interaction with the divertor structures, as used in [26, 27].

C. DKES

The neoclassical part of the particle and energy transport can be calculated with transport coefficients derived from a drift-kinetic description of the plasma. The so-called Drift-Kinetic Equation (DKE) [35] allows a steady-state solution for the distribution function f, which is assumed to differ from the local Maxwellian distribution function f_{M} only by a "small" perturbation $f_1 = f - f_{\mathrm{M}}$. The DKE for f_1 can be linearized on the assumption that the transport processes are radially (on flux surfaces) local. For an expression of the linearized DKE allowing it to assume a so-called mono-energetic form see [36]. Thus the initially 5-dimensional DKE can be reduced by 2 dimensions, since the corresponding variables, flux surface label and particle energy, appear only as parameters, thus simplifying the numerical treatment. To allow the mono-energetic ansatz, energy diffusion is neglected in the collision operator and only pitch-angle scattering is retained. This has no consequences for the radial transport in stellarators but causes errors for the parallel transport (along field lines) because it violates parallel momentum conservation. However, techniques for parallel momentum correction are available [37] to cure this deficiency in the parallel flows at a later stage and thereby recover correct results.

The solution of the DKE, which is numerically calculated with the DKES code, is used to obtain the transport coefficients for fluxes or flows through (radial) or within (parallel) a flux surface by integrating the properly weighted perturbation of the distribution function over the remaining 3 dimensions, i. e. the pitch angle and the two angular coordinates (flux surface average). The resulting so-called mono-energetic transport coefficients $D_{ij}^{(\alpha)}$ of each particle species α

$$D_{ij}^{(\alpha)} = D_{ij}^{(\alpha)}\left(r, \frac{\nu_\alpha}{v_\alpha}, \frac{E_r}{v_\alpha B_0}\right) \tag{5}$$

capture the transport properties of particles with a specific energy, thus the designation. Here, ν_α, v_α, E_r and B_0 are the collision frequency, velocity (corresponding to the chosen energy), radial electric field and magnetic field, respectively [31]. The flux-surface-averaged flows $I_i^{(\alpha)}$ and the thermodynamic forces $A_j^{(\alpha)}$ driving these flows can then be written as

$$I_i^{(\alpha)} = -n^{(\alpha)} \sum_{j=1}^{3} L_{ij}^{(\alpha)} A_j^{(\alpha)}, \tag{6}$$

where $n^{(\alpha)}$ is the particle density, $I_1^{(\alpha)}$ is related to the radial particle flux density, $I_2^{(\alpha)}$ to the radial energy flux density, and $I_3^{(\alpha)}$ to the toroidal current density (for stellarators without an externally imposed electric field this is essentially the bootstrap current — for exact definitions see [36]).

The so-called thermal transport coefficients $L_{ij}^{(\alpha)}$ are calculated from the mono-energetic ones by an energy convolution with a local Maxwellian with appropriate energy weightings (see also [36]).

For each magnetic configuration calculated with VMEC, a table of mono-energetic transport coefficients $D_{ij}^{(\alpha)}$ is generated, reflecting the dependances shown in Eq. (5) to allow a fast convolution for arbitrary plasma parameters in a 1D transport simulation code like NTSS. The generation of these DKES tables (for several minor radii, collisionalities and radial electric field values) is the most computationally expensive step of the entire iteration cycle, in particular the calculations for low collisionalities. Nevertheless, since the tables are later used in interpolating functions, the results need to be checked manually for their quality and suitability, especially the low-collisionality values. This is currently a necessary part of the cycle.

D. NTSS

The NTSS code has been designed to solve the time-dependent set of transport equations encompassing the particle and energy balance of electrons and ions together with a diffusion equation for the radial electric field E_r and an equation for the evolution of the poloidal flux, the latter being equivalent to the evolution of the toroidal current density [17, 31]. For our purpose, we use only the ability to provide the stationary solutions of these equations. In particluar, we do not solve the time evolution of the toroidal current density or poloidal flux but only use the calculated bootstrap current distribution resulting from the transport coefficients and plasma profiles.

Particle and energy balance equations contain on the one hand the neoclassical transport, based on first principles (see [31]), using the transport coefficients calculated with DKES. On the other hand NTSS uses heuristic models to account for the turbulence-driven, so-called anomalous, transport. This is simulated just by a simple diffusion model, where the heat diffusion coefficient is, in our case, $\chi_{\text{base}} = 1\,\text{m}^2\text{s}^{-1}$ at the boundary of the model region and is inversely proportional to the density. This model serves two purposes: first, allowing sufficient transport at the plasma boundary, where neoclassical transport is far too low to produce reasonable temperatures, and second, ensuring that neoclassical transport will display its performance limiting role in the core plasma. The model is based on certain high-performance experiments in the Wendelstein 7-AS stellarator, which showed a core region with a dominantly neoclassical transport [38, sections 3.3 and 5.3.2].

In the NTSS simulations used here, the particle balance equation is not solved, but the density profile is kept fixed (see Fig. 5), since the modelling of particle sources would require the coupling with further codes. Because the density profile has been chosen rather broad, this results in a fast decay of the anomalous contribution in the energy balance equation to about a tenth of the boundary value in most of the plasma volume.

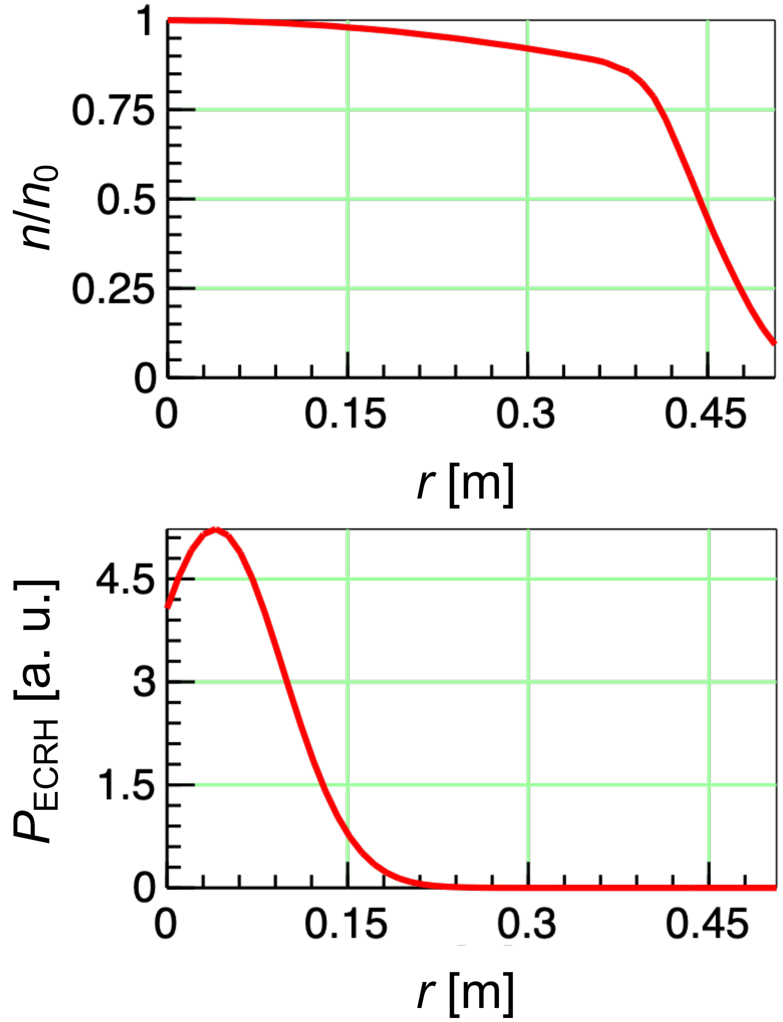

FIG. 5: Fixed density (top) and heating power (bottom) profiles used in the NTSS simulations.

We aim at a high-performance plasma scenario at high density, requiring ECR O2-mode heating, which in turn asks for central deposition for high electron temperatures and relies on a three-path absorption, fixing the launching angles of the beams [39]. For the power deposition profile we therefore use a fixed standard profile approximating the real O2 deposition profile with sufficient accuracy (see Fig. 5). Other heating methods with different power deposition profiles are not considered here.

The calculation of E_r is performed with a diffusion equation to avoid the discontinuities which occur for the non-linear ambipolarity condition $Z_{\mathrm{i}}\Gamma_{\mathrm{i}} = \Gamma_{\mathrm{e}}$ (balancing ion and electron particle fluxes $\Gamma_{\mathrm{i/e}}$) at a bifurcation point where electron-root and ion-root solutions are interchanged.

The bootstrap current is calculated from the parallel neoclassical flows and can be used in the time-dependent version in the evolution of the poloidal flux (equivalent to the toroidal current density — see [17] for details). As stated before, using the DKES transport coefficients for the parallel transport equations requires the use of momentum correction techniques [37]. These are implemented in NTSS.

Thus, in principle, given sources and sinks for particles, energy and current (e. g. by ECCD), NTSS can calculate the the time evolution of the radial profiles of electron and ion density and temperature, of the radial electric field and of the bootstrap current. As stated before, we omit the solution of the particle transport equation in this work and instead keep the density profile fixed, and we only consider stationary solutions. One should note, that these calculated profiles depend on

1. the MHD equilibrium, through the configuration dependency in the DKES calculation,
2. the assumed experimental scenario with density and heating and
3. the anomalous transport model.

E. Iterative Modelling for consistency between magnetic configuration, neoclassical transport and radial profiles

As indicated in section III A, part of the input and output of the three codes VMEC, DKES and NTSS cyclically depend on each other. We start the cycle by assuming initial profiles for pressure and toroidal current density $p_{\mathrm{in}(1)}(s) = p_{\mathrm{ini}}(s)$ and $j_{\mathrm{tor,in}(1)}(s) = j_{\mathrm{tor,ini}}(s)$, where $j_{\mathrm{tor}}(s)$ represents the toroidal net current density, averaged on the flux surface with label s. In terms of VMEC's numerical procedure,

$$\frac{\mathrm{d}I_{\mathrm{tor}}(s)}{\mathrm{d}s} = j_{\mathrm{tor}}(s)\,\frac{\mathrm{d}A}{\mathrm{d}s} \tag{7}$$

is used rather than $j_{\mathrm{tor}}(s)$, where $I_{\mathrm{tor}}(s)$ is the total toroidal current inside the flux surface with label s, and $A(s)$ is the toroidally averaged cross-sectional area of this flux surface. VMEC uses this input only for the functional shape of the profile and scales it to obtain the target value of the bootstrap current $I_{\mathrm{bs,target}}$, which is a separate input. For the sake of simplicity, we shall here refer to $j_{\mathrm{tor}}(s)$ as input profile of the toroidal current density, which satisfies

$$\int\limits_0^1 j_{\mathrm{tor,ini}}(s)\,\frac{\mathrm{d}A}{\mathrm{d}s}\,\mathrm{d}s = I_{\mathrm{bs,target}}. \tag{8}$$

A VMEC run under these assumptions yields a magnetic equilibrium configuration, which is used to obtain from DKES a table of mono-energetic neoclassical transport coefficients, as described in section III C. The magnetic configuration from VMEC and the transport coefficients from DKES are then used for a number of NTSS simulation runs with the same heating power P and power deposition profiles, the same predefined density profile shape, but different values of the central density n_0. In addition, anomalous transport is simulated in the NTSS runs by a predefined heat diffusivity (see section III D).

The result after iteration cycle no. k are new pressure and toroidal current density profiles $p_{(k)}(s)[P, n_0]$ and $j_{\mathrm{tor},(k)}(s)[P, n_0]$, withdifferent values of the bootstrap current

$$\int\limits_0^1 j_{\mathrm{tor},(k)}(s)[P, n_0]\,\frac{\mathrm{d}A}{\mathrm{d}s}\,\mathrm{d}s = I_{\mathrm{bs},(k)}[P, n_0]. \tag{9}$$

For the next iteration $k+1$, we choose the profile shapes of that density value n_0, for which $I_{\mathrm{bs},(k)}$ is closest to the target value of the bootstrap current $I_{\mathrm{bs,target}}$. We denote the selected value of n_0 as $n_{0,\mathrm{base}(k)}$. The iterations are performed separately for each value of P, and also $I_{\mathrm{bs,target}}$ may differ for different values of P. For the next VMEC run, we use, instead of $I_{\mathrm{bs},(k)}[P, n_{0,\mathrm{base}(k)}]$, again $I_{\mathrm{bs,target}}$ as input for the total toroidal current since this is the target value of the entire iteration: The configuration calculated by VMEC will thus change between iterations only due to the different profile shape, and the rotational transform at the boundary of the VMEC domain will only change very little between iterations. Hence, for the next iteration cycle, the input profiles for VMEC are

$$p_{\mathrm{in}(k+1)}(s)[P] = p_{(k)}(s)[P, n_{0,\mathrm{base}(k)}] \tag{10}$$

$$j_{\mathrm{tor,in}(k+1)}(s)[P] = \frac{I_{\mathrm{bs,target}}}{I_{\mathrm{bs},(k)}[P, n_{0,\mathrm{base}(k)}]} \times j_{\mathrm{tor},(k)}(s)[P, n_{0,\mathrm{base}(k)}]. \tag{11}$$

From the new VMEC equilibrium, a new table of neoclassical transport coefficients is generated by DKES. NTSS is run next for a range of n_0 values around $n_{0,\mathrm{base}(k)}[P]$, possibly including an interpolated value of n_0 to more closely hit $I_{\mathrm{bs,target}}$ in the result.

In section IV A, we shall present the resulting bootstrap current $I_{\mathrm{bs},(1)}[P, n_0]$ of the first iteration cycle for a broad range of (P, n_0) values to show the general dependance on these parameters. We shall then proceed up to the 4th iteration cycle for selected power steps to demonstrate that the convergence of the profiles and of I_{bs} to the desired target value is achieved in our procedure.

F. Field Line Diffusion and Assessment of Critical Regions

To calculate the heat load on different regions of the divertor and other plasma facing components (PFCs), the technique of field line diffusion is used, as described, e. g., in [32, 40]. To this end, a number N_{tot} of starting points is chosen, which are distributed uniformly on a flux surface a few millimeters inside the last closed magnetic surface. From each starting point, the magnetic field lines are followed in both directions with small random perpendicular steps taken to imitate perpendicular diffusion. The parameters to describe this diffusion process and their values chosen for this work are the diffusion coefficient $D_\perp = 1\,\mathrm{m^2 s^{-1}}$, the scale of the path length between two perpendicular steps $\lambda = 0.1\,\mathrm{m}$ and the parallel "velocity" (which, together with $D_\perp$, determines the ratio between parallel and perpendicular transport) $v = 5 \times 10^5\,\mathrm{ms^{-1}}$. Each trace is followed until it intersects a PFC. The location of each such hit point is recorded.

To calculate the power density, an appropriate segmentation of the PFCs is chosen, and for each segment i the number of hits on this segment N_i is divided by the segment area A_i. The power density on this segment is therefore calculated as

$$q_i = \frac{N_i P_{\mathrm{conv}}}{N_{\mathrm{tot}} A_i}, \tag{12}$$

where P_{conv} is the total available convective power [41] (e. g., for a worst-case estimate, the total heating power). Here, the segmentation size is chosen small enough to resolve the regions of the PFCs with different technical heat flux limits and the scale size of the heat load patterns. For the target plates, mostly segments corresponding to the individual tiles on the high heat flux target elements (with a typical size of 50 mm × 25 mm) are chosen. The calculated power loads q_i are compared to the maximum design heat load $q_{\mathrm{d},\,i}$ (see Table II and Fig. 6). Note the sides facing the pumping gap, where the reduced $q_{\mathrm{d},\,i}$ values are critical from the overload analysis point of view.

TABLE II: Technical limits $q_{\mathrm{d},\,i}$ for target components in W7-X [42].

Component	$q_{\mathrm{d},\,i}$ [MW/m^2]
High loaded area	10.0
- End Top Tile	5.0
- Edge Tile	2.0
Lower loaded area	0.5

The ratio $q_i/q_{\mathrm{d},\,i}$ together with the number of hits N_i out of N_{tot}, on which q_i is based, can be used for a statistical analysis of the probability of overloading a particular segment [41].

IV. RESULTS

A. Bootstrap Current for Variation of Density and Heating Power

To show the general trends, we started one iteration cycle by creating MHD equilibria with VMEC, based on a vacuum magnetic field generated by the coil currents of Table I, assuming a linear pressure profile

$$p_{\mathrm{ini}}(s) = p_{\mathrm{c}}(1-s) \tag{13}$$

and a parabolic current profile

$$j_{\mathrm{tor,ini,A}}(s) = j_{\mathrm{c,A}}\, s(1-s) \tag{14}$$

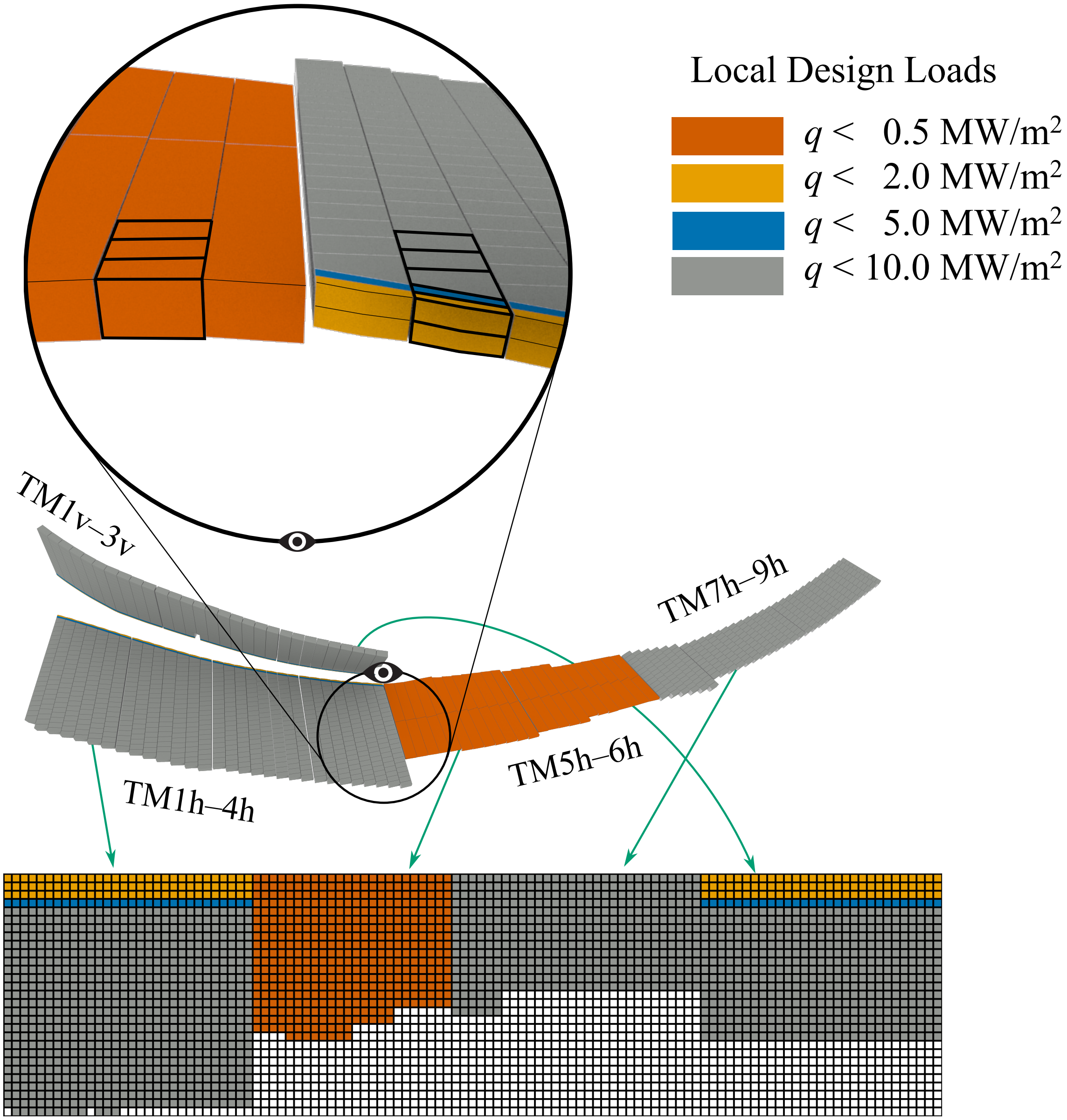
Local Design Loads
$q <$ 0.5 MW/m^2
$q <$ 2.0 MW/m^2
$q <$ 5.0 MW/m^2
$q <$ 10.0 MW/m^2
TM1v–3v
TM7h–9h
TM5h–6h
TM1h–4h

FIG. 6: Mapping of a divertor unit to a 2D grid, as used for representing the power density in section IV. The colors indicate the maximum design heat load (Table II) for each surface element [41]. The magnified view from the inboard shows in particular the critical region adjacent to the pumping gap in a golden-orange color.

with p_c and $j_{c,A}$ chosen such that the $\langle\beta\rangle$ value is 2 % or 3 % and the total toroidal current is $I_{bs,target} = 30\,\mathrm{kA}$. Mono-energetic neoclassical transport coefficients were calculated for these equilibria and used in NTSS for a range of central densities n_0 and heating powers P. The resulting bootstrap currents $I_{bs,(1),A}[P, n_0]$ are shown in Fig. 7. Following the 30 kA

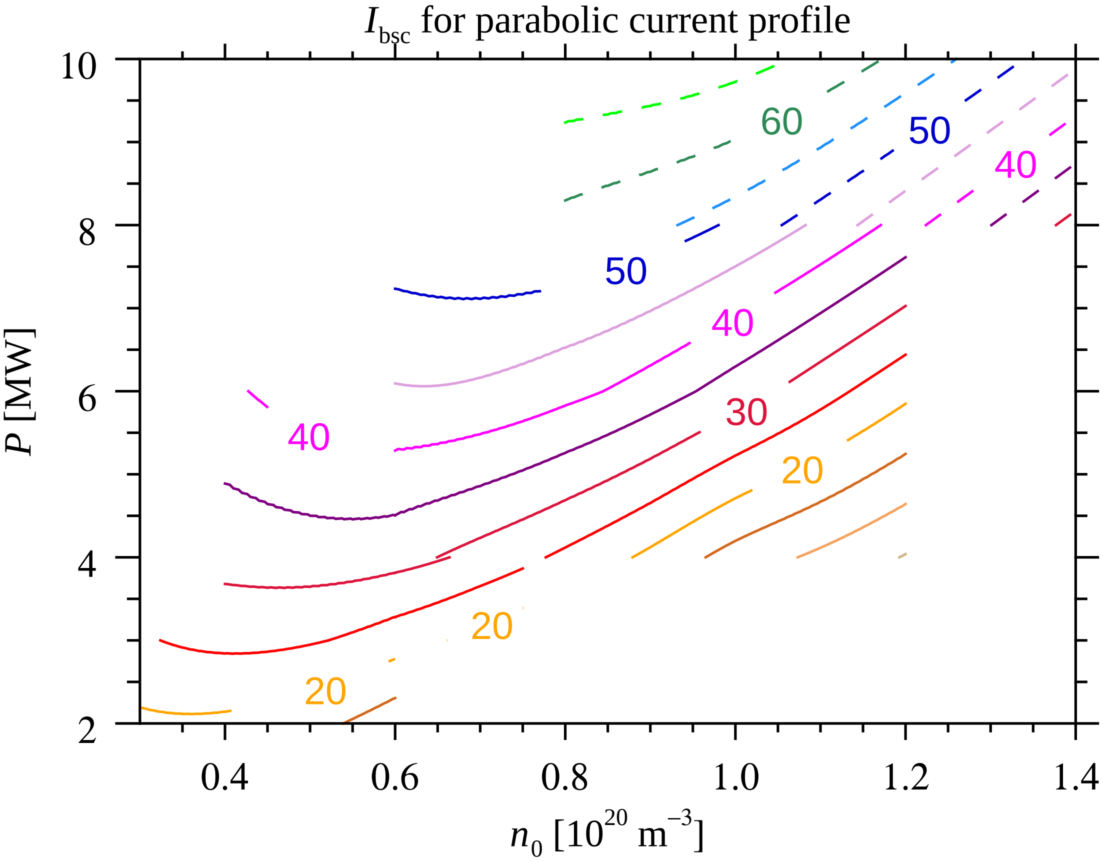

FIG. 7: Bootstrap current after first iteration cycle, starting from a linear pressure profile and a parabolic profile of the toroidal current density. The resulting values ($I_{\mathrm{bs},(1),\mathrm{A}}$) are indicated in kA at the contour levels. The calculations represented by solid (dashed) lines are performed for MHD equilibria with $\langle\beta\rangle$ of 2 (3) %. For the further assumptions, see text.

contour in that figure would outline a path from low power (ca. 4 MW) and low density (0.4 to 0.6 × $10^{20}\,\mathrm{m}^{-3}$) to high power (8 MW) and high density (1.4 × $10^{20}\,\mathrm{m}^{-3}$) without significant changes in the edge rotational transform.

However, the resulting profiles $p_{(1)}(s)$ and $j_{\mathrm{tor},(1)}(s)$ are different from the initial profiles and different for each set (P, n_0). In particular, the current density profiles in the NTSS results show a more centrally peaked form. Since the bootstrap current also depends on the profile of ι and different current density profiles result in different ι profiles, the hope was to achieve faster convergence with a more educated guess for the profile shapes. Before continuing the iteration (section IV B), we therefore investigate the effect of starting with a more peaked choice for the profile of the toroidal current density,

$$j_{\mathrm{tor,ini,B}}(s) = j_{\mathrm{c,B}}\, s\{0.1(1-s) + (1-s)^2 + 10(1-s)^8\}, \tag{15}$$

with $j_{\mathrm{c,B}}$ again chosen such that the total toroidal current is 30 kA. This function is displayed in Fig. 9 (top panel) as 'modified profile'. However, a rather similar behaviour of the resulting bootstrap current $I_{\mathrm{bs},(1),\mathrm{B}}[P, n_0]$ is found as that of $I_{\mathrm{bs},(1),\mathrm{A}}$ depicted in Fig. 7. The 30 kA contour is only slightly shifted in the (P, n_0) plane. In Fig. 8, we show the differences $I_{\mathrm{bs},(1),\mathrm{A}} - I_{\mathrm{bs},(1),\mathrm{B}}$ in the (P, n_0) plane.

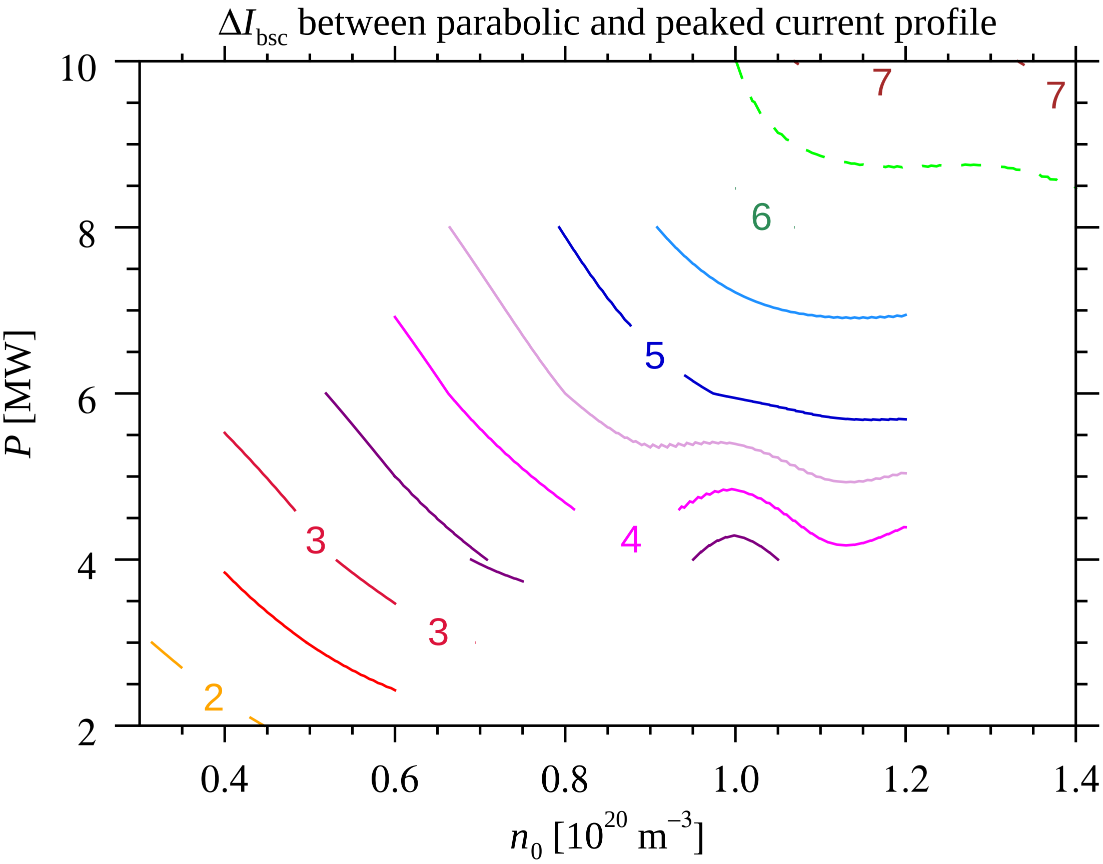

FIG. 8: Differences of the resulting bootstrap current after the first iteration cycle for start with a parabolic and a peaked profile of the toroidal current density, $I_{\mathrm{bs},(1),\mathrm{A}} - I_{\mathrm{bs},(1),\mathrm{B}}$.

B. Convergence of pressure and current density profiles

As described in section III E, for the initial VMEC run, guessed profiles for pressure and toroidal current density, $p_{\mathrm{ini}}(s)$ and $j_{\mathrm{tor,ini}}(s)$, are chosen. After cycling through DKES and

TABLE III: Convergence of successive iterations of the radial profiles $f_{(k)}(s)$, quantified by a measure D_k.

$$D_k \equiv \frac{\sqrt{\sum\limits_{i=1}^{N} (f_k(s_i) - f_{k-1}(s_i))^2}}{\sqrt{\sum\limits_{i=1}^{N} (f_{k-1}(s_i))^2}}$$

$f(s)$	$j_{\mathrm{tor}}(s)$	$p(s)$
D_1	0.0311	0.0608
D_2	0.019	0.0026
D_3	0.008	0.0017
D_4	0.0017	0.00015

NTSS, we arrive at a set of different profiles, depending on the P and n_0 values chosen in NTSS. In iteration no. k, each profile has a different total current $I_{\mathrm{bs},(k)}[P, n_0]$. The input profiles for the next iteration for a given value of P is decided based on the value of $I_{\mathrm{bs},(k)}$ closest to 30 kA. As an example, we demonstrate in Fig. 9 the convergence of the profiles for a heating power of $P = 8\,\mathrm{MW}$. After 4 iterations, the profiles do no longer change visibly (see Table III), and a solution with consistent input and output of the three codes is reached.

C. Path to High Performance

We have computed such self-consistent solutions for heating powers of 2, 4, 6, 8 and 10 MW. From these, we assemble a final path starting at $P = 2\,\mathrm{MW}$, $n_0 = 0.4 \times 10^{20}\,\mathrm{m}^{-3}$ with $I_{\mathrm{bs}} = 17\,\mathrm{kA}$. Heating power and density are then increased to (4 MW, $0.6 \times 10^{20}\,\mathrm{m}^{-3}$) with $I_{\mathrm{bs}} = 28\,\mathrm{kA}$ and to (6 MW, $1.0 \times 10^{20}\,\mathrm{m}^{-3}$) with $I_{\mathrm{bs}} = 30\,\mathrm{kA}$. After this point, I_{bs} can be kept constant by a coordinated increase of heating power and density through (8 MW, $1.31 \times 10^{20}\,\mathrm{m}^{-3}$) to (10 MW, $1.57 \times 10^{20}\,\mathrm{m}^{-3}$). The whole path is represented in Fig. 10, together with further operation points for each power step from our parameter scan.

The L/R times for the 2 MW and 4 MW cases are 20–40 s. This is the time scale required to achieve the I_{bs} target value. The time scale for changes in the total toroidal current remains on the same order of magnitude for the subsequent plasma states, but the transition

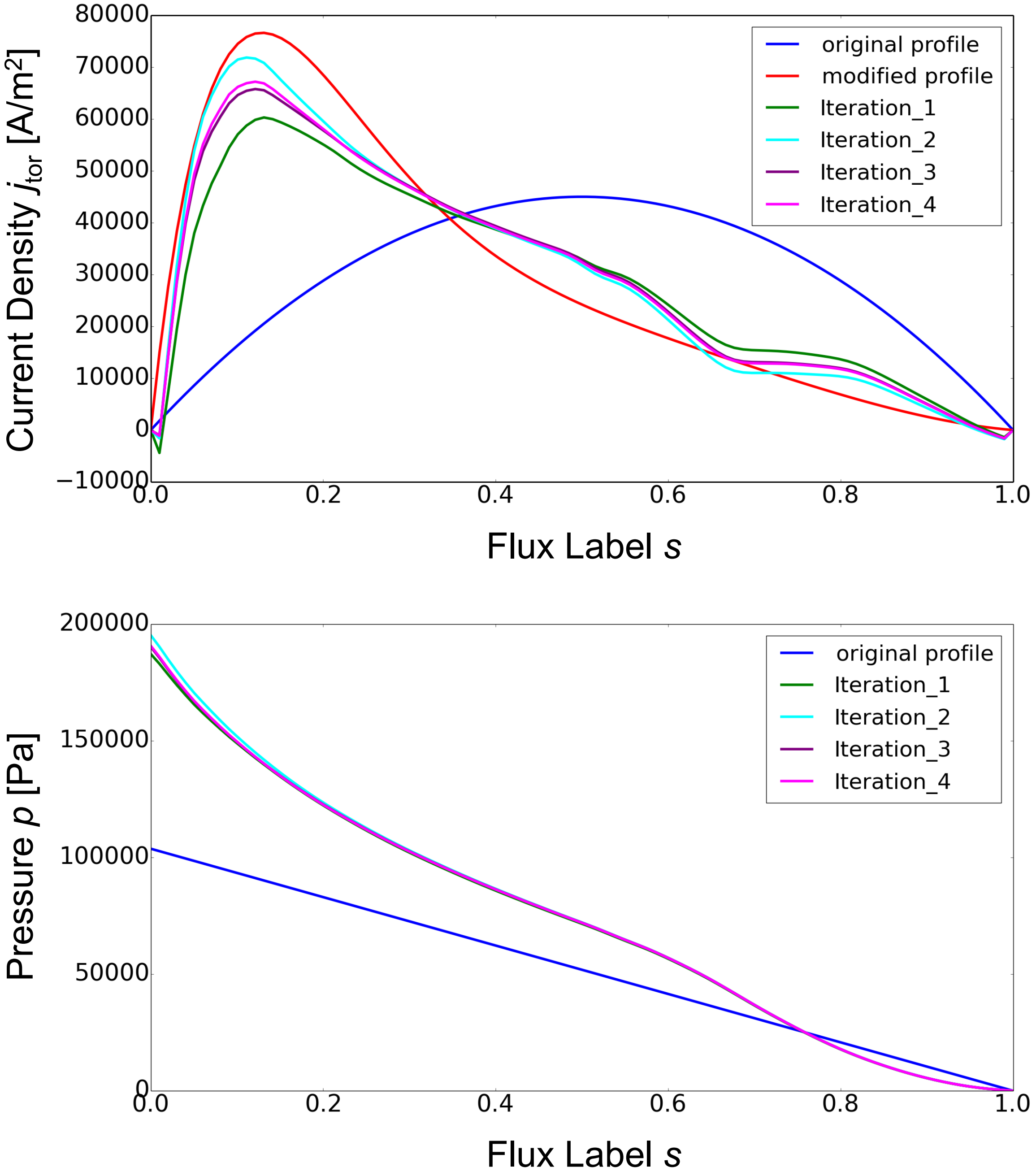

FIG. 9: Evolution of the radial profiles of toroidal current density $j_{\mathrm{tor}}(s)$ (top) and pressure $p(s)$ (bottom) for a heating power of $P = 8\,\mathrm{MW}$ and 4 iteration cycles. The iteration procedure is described in section III E. For $j_{\mathrm{tor}}(s)$ the two initial profiles $j_{\mathrm{tor,ini,A}}$ ("original profile") and $j_{\mathrm{tor,ini,B}}$ ("modified profile") are shown.

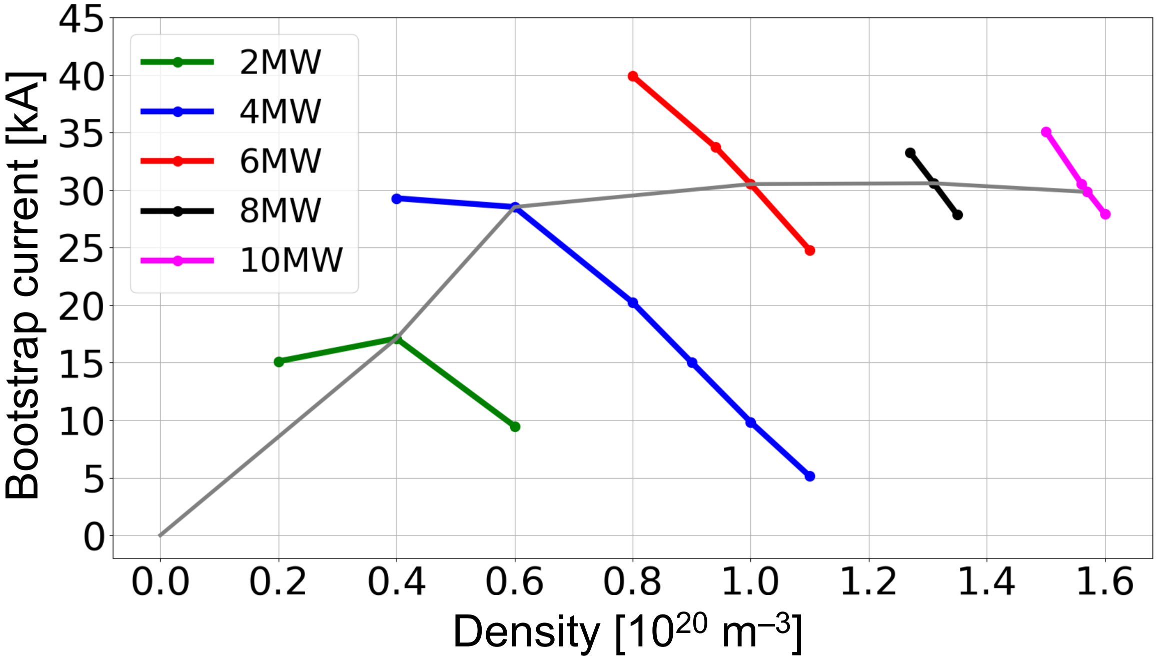

FIG. 10: Stationary values of the bootstrap current on the final path (in grey) from low power and low density toward high power and high density. For each power step, the bootstrap currents for the neighbouring values of the density n_0 are also displayed (in colours).

to higher density and heating power can be faster, since I_{bs} does no longer change. Should the evolution of the discharge deviate from the planned path, sufficient time (L/R) is available to switch off the heating before the island geometry is modified in a way to endanger the sensitive areas of the targets.

For a fixed heating power, the plasma density cannot be chosen arbitrarily high. Due to edge radiation, there exists a density limit n_{c} in stellarators, which can be described by the empirical scaling

$$n_{\mathrm{c}} = c_{\mathrm{conf}} \frac{P^{0.6}}{{f_{\mathrm{imp}}}^{0.4}} \tag{16}$$

for W7-X [43]. Here, n_{c} is the line-averaged electron density in $10^{19}\,\mathrm{m}^{-3}$, P is the heating power in MW, f_{imp} is the impurity fraction and c_{conf} is a numerical factor, which depends weakly on the magnetic configuration and is ~ 0.56 in our case. In Table IV we compare the line-averaged densities on our discharge path with n_{c} for an impurity fraction of $1\,\%$, which was found to be a realistic value in the most recent operation phase of W7-X after boronization [43]. We note that the (P, n_0) values on our path do not violate the limit of

TABLE IV: Comparison of line-averaged densities $\bar{n}$ with the empirical density limit n_c of Eq. (16) [43], assuming an impurity fraction of 1 %.

P [MW]	2	4	6	8	10
n_0 [$10^{19}\,\mathrm{m}^{-3}$]	4	6	10	13.1	15.7
$\bar{n}/n_\mathrm{c}$	0.63	0.62	0.81	0.90	0.94

Eq. (16).

The magnetic configurations of the chosen path were provided as full fields (i. e., including the effects of the plasma currents) with VMEC-EXTENDER (see section III B) and were used to calculate the power load to the divertor within the field line diffusion model (see Fig. 11). The predicted heat load for the divertor at the edges near the pumping gap is well within the design limits given in section III F for all five magnetic configurations, since the configuration with a bootstrap current of 17 kA, which places the strike line to an area with reduced design load at the edge of the pumping gap, is passed at low heating power (2 MW, 1/5 the final power).

We also compared the neoclassical transport properties in the lmfp regime between the 10 MW configuration of our path and the SE reference configuration proposed in [27] (see Table I for the coil currents). Fig. 12 shows the radial profiles of the effective helical ripple ε_eff [36], the corresponding figure of merit, which demonstrates that both configurations have very similar neoclassical transport properties, in the vacuum configuration as well as in the version with finite β and bootstrap current.

V. DISCUSSION

The discharge scenario and the path from plasma startup to a high-performance plasma presented in this work are of a “proof-of-principle” type: The simulations are based on a number of assumptions, like the neglect of radiation effects, the fixed shape of the density profile, or the diffusive ansatz for anomalous transport and the value of the corresponding heat diffusion coefficient.

Whereas neoclassical transport is based on a theory derived from first principles, the anomalous transport in W7-X has still to be explored and described experimentally as

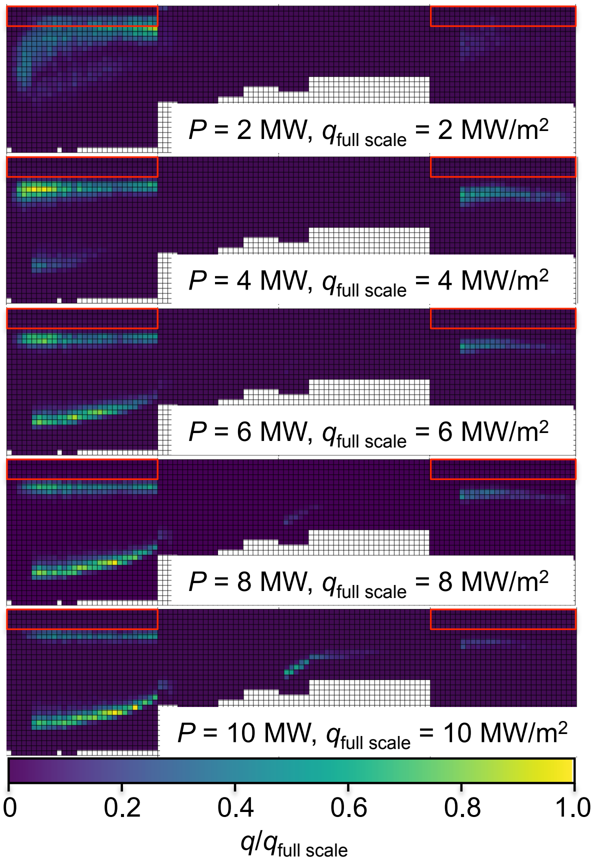

FIG. 11: Heat load patterns on the targets for different heating power P. For each value of P, the magnetic configuration from the last iteration of VMEC+EXTENDER was used for field line diffusion with 20 000 starting points. The targets are represented as introduced in Fig. 6, and we have marked the areas with reduced design load by red rectangles. The color scale is adapted to the heating power for a better visibility of the changes in the heat load pattern.

well as theoretically. Although the physical mechanism of anomalous transport is generally believed to be turbulence rather than diffusion, diffusion with an empirical coefficient is widely used in transport codes to simulate it. Our choice, as introduced in section III D, is motivated by observations in various devices, as summarized, e. g., in [44, p. 548] as anomalous electron heat diffusion coefficient $\chi_{\mathrm{e}} = C/n$ with $C = (1 \ldots 5) \times 10^{-19}\,\mathrm{m}^{-1}\mathrm{s}^{-1}$. Likewise, on Wendelstein 7-AS, the comparison between measured temperature profiles and predictions of neoclassical transport indicated dominating anomalous heat transport in the edge, and the values of the inferred anomalous heat diffusion coefficients were of the same order of magnitude and they displayed a similar radial dependance [45, section III] as used

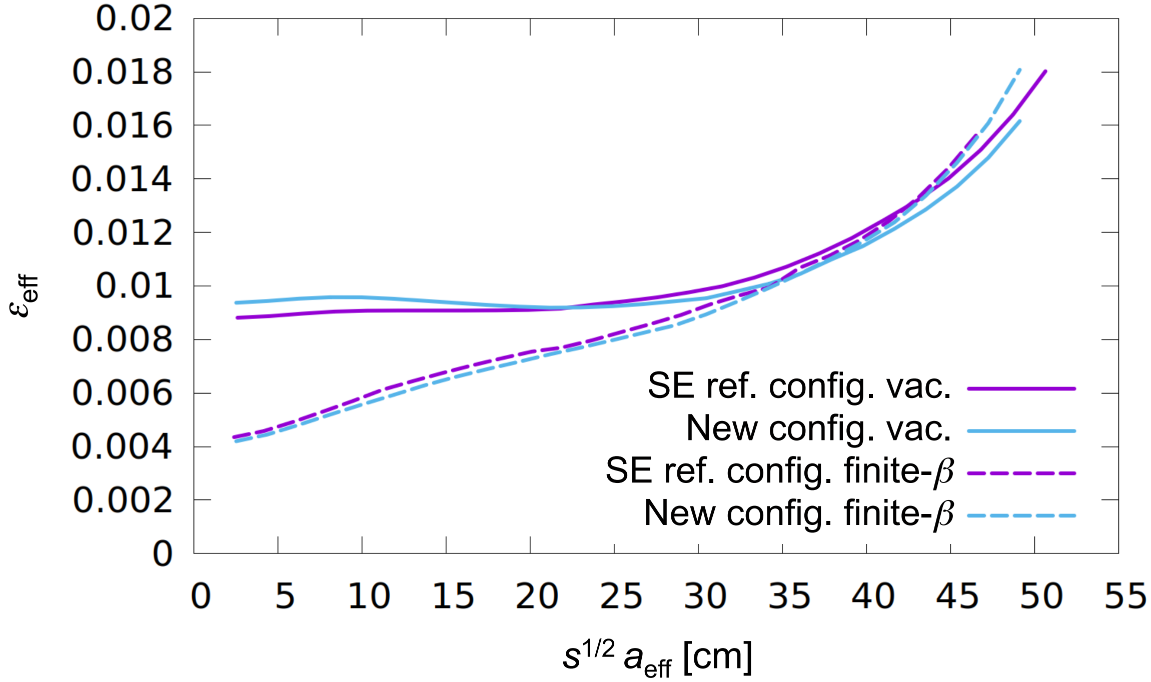

FIG. 12: Comparison of $\varepsilon_{\mathrm{eff}}$ between the vacuum versions and the finite-β versions of the scraper element (SE) reference configuration with 43 kA bootstrap current and our newly developed configuration with 30 kA bootstrap current and 10 MW heating power. Neither the vacuum versions nor the finite-β versions show significant differences.

in NTSS for the present study.

To investigate the impact of different values of the anomalous transport coefficient, we increased the base value from $1\,\mathrm{m}^2/\mathrm{s}$ to 2 and $4\,\mathrm{m}^2/\mathrm{s}$ in NTSS, without performing the iteration cycle to obtain consistent magnetic configurations with VMEC and new mono-energetic transport coefficients with DKES. As expected, the central temperatures were reduced, and we obtained lower values for the bootstrap current (see Table V). On the other hand side, we find that a bootstrap current of 30 kA can be achieved if the heating power is increased from 8 MW to 10.6 MW (16.8 MW) for $\chi_{\mathrm{base}} = 2\,\mathrm{m}^2/\mathrm{s}$ ($4\,\mathrm{m}^2/\mathrm{s}$) in the case with $n_0 = 1.31 \times 10^{20}\,\mathrm{m}^{-3}$, or from 10 MW to 13.9 MW (20.9 MW) for $\chi_{\mathrm{base}} = 2\,\mathrm{m}^2/\mathrm{s}$ ($4\,\mathrm{m}^2/\mathrm{s}$) in the case with $n_0 = 1.57 \times 10^{20}\,\mathrm{m}^{-3}$ (all cases of this sensitivity study were calculated in NTSS with the density, magnetic configuration and mono-energetic transport coefficients of the corresponding $1\,\mathrm{m}^2/\mathrm{s}$ base cases, without iterating VMEC, DKES and NTSS for consistency).

Changing the anomalous transport will affect the simulation results in various ways, i. e.,

TABLE V: Variation of the heat diffusion coefficient in NTSS for the two last steps on the path of section IV C (without iterating with VMEC and DKES for consistent results). The $1/n$ dependance is retained, but the base value at the boundary of the computation domain is chosen as listed. The indirect effect of an increased radial heat diffusivity on the bootstrap current is similar to the effect of an increase in density.

χ_{base} [m^2/s]	$P = 8\,\text{MW}$, $n_0 = 1.31 \times 10^{20}\,\text{m}^{-3}$		$P = 10\,\text{MW}$, $n_0 = 1.57 \times 10^{20}\,\text{m}^{-3}$	
	$\langle\beta\rangle$ [%]	I_{bs} [kA]	$\langle\beta\rangle$ [%]	I_{bs} [kA]
1	3.1	30.6	3.6	30.5
2	2.4	9.3	2.8	6.3
4	1.6	−5.7	1.9	−9.3

via the equilibrium, through the different collisionalities due to changed profiles and the radial electric field, and via the convolution of the mono-energetic transport coefficients with the Maxwellian. It should be noted that the bootstrap current itself is a purely neoclassical effect, without anomalous contribution. The lower value of I_{bs} with increased anomalous transport in our model is therefore entirely due to the indirect effects of reduced temperatures and changed profiles. For the magnetic configuration under consideration, an increase of the anomalous transport at fixed heating power has a similar effect as an increase in plasma density.

We note that the plasma-pressure-induced currents can also modify the magnetic boundary structure by changing the island size. This MHD-equilibrium effect is included in our simulation through the use of the magnetic configurations calculated by VMEC-EXTENDER. For our case with a boundary ι of 5/5, the island size increases with increasing β (see, e. g., [46, Fig. 1]). Non-MHD-equilibrium effects influencing the island size (as observed in LHD, leading to island healing [47]) are not considered here, since they apply to internal islands and not to islands intersected by divertor structures.

VI. CONCLUSION

Although W7-X is optimized for low bootstrap current operation, the remaining toroidal net current of up to several 10 kA has long been identified as a challenge for the operation of the island divertor [17]. In particular, the slow evolution of the toroidal net current on the time scale of several tens of seconds may, in a high-power discharge, thermally overload regions of the target plates close to the pumping gap, which are rated for reduced power load. Different solutions to this problem were already proposed, as listed in section II.

In this paper, we demonstrated in a numerical proof-of-principle study, in the framework of neoclassical theory, and assuming a certain amount of anomalous transport, that the dependance of the bootstrap current on the profile shapes can be utilized to keep the bootstrap current constant over a wide range of density and heating power, as long as both quantities are varied in a coordinated way. Even in a magnetic configuration displaying a bootstrap current which needs compensation to allow proper divertor operation, it is thus in principle possible to find a non-critical path toward high plasma density at high heating power without overloading the edges of the targets at the pumping gap, and without the need to feedback-control the superconducting field coils, to apply ECCD, or to install costly additional target components. In contrast to most previous studies of this topic, we verified that our results remain valid if mutually consistent magnetic configurations, neoclassical transport coefficients and radial profiles of plasma pressure and toroidal current density are used. We note that the density values of our path are also below the empirical density limit of W7-X [43] for each power step.

A number of simplifying assumptions were made in this study, such that, in reality, the bootstrap current may assume substantially different values from our simulation results. In particular, a different amount of anomalous transport or different power deposition profiles will modify the radial temperature profiles. Likewise, the density profile may deviate from the assumed fixed shape. Nevertheless, as soon as the model assumptions are adapted appropriately by comparison with observations or by advances in theory, the scheme in itself allows to predict whether such a safe path to a desired operation point exists. A coordinated control of plasma density and heating power, guided by such calculations as ours as well as by experimental experience, could well prove to be an effective and attractive approach to control the bootstrap current evolution, and thereby control the dynamics of the divertor heat load patterns. A comparison with experimental observations will be the logical continuation of this work.

ACKNOWLEDGEMENTS

We would like to thank S. Bozhenkov for his help with the IPP Webservices and C. D. Beidler for instructive discussions on neoclassical theory.

This work has been carried out within the framework of the EUROfusion Consortium and has received funding from the Euratom research and training programme 2014–2018 and 2019–2020 under grant agreement No 633053. The views and opinions expressed herein do not necessarily reflect those of the European Commission.

---

[*] email: priyanjana.sinha@ipp.mpg.de

[1] G. Grieger, C. Beidler, E. Harmeyer, W. Lotz, J. Kißlinger, P. Merkel, J. Nührenberg, F. Rau, E. Strumberger, and H. Wobig, Fusion Technology **21**, 1767 (1992).

[2] H.-S. Bosch *et al.*, Nucl. Fusion **53**, 126001 (2013).

[3] V. Erckmann, P. Brand, H. Braune, G. Dammertz, G. Gantenbein, W. Kasparek, H. P. Laqua, H. Maassberg, N. B. Marushchenko, G. Michel, M. Thumm, Y. Turkin, M. Weissgerber, A. Weller, W7-X ECRH Team at IPP Greifswald, W7-X ECRH Team at FZK Karlsruhe, and W7-X ECRH Team at IPF Stuttgart, **52**, 291 (2007).

[4] R. C. Wolf, S. Bozhenkov, A. Dinklage, G. Fuchert, Y. O. Kazakov, H. P. Laqua, S. Marsen, N. B. Marushchenko, T. Stange, M. Zanini, I. Abramovic, A. Alonso, J. Baldzuhn, M. Beurskens, C. D. Beidler, H. Braune, K. J. Brunner, N. Chaudhary, H. Damm, P. Drewelow, G. Gantenbein, Y. Gao, J. Geiger, M. Hirsch, U. Höfel, M. Jakubowski, J. Jelonnek, T. Jensen, W. Kasparek, J. Knauer, S. B. Korsholm, A. Langenberg, C. Lechte, F. Leipold, H. Trimino Mora, U. Neuner, S. K. Nielsen, D. Moseev, H. Oosterbeek, N. Pablant, E. Pasch, B. Plaum, T. Sunn Pedersen, A. Puig Sitjes, K. Rahbarnia, J. Rasmussen, M. Salewski, J. Schilling, E. Scott, M. Stejner, H. Thomsen, M. Thumm, Y. Turkin, F. Wilde, and Wendelstein 7-X Team, Plasma Phys. & Controlled Fusion **61**, 014037 (2019).

[5] H. P. Laqua, H. Maassberg, N. B. Marushchenko, F. Volpe, A. Weller, W7-AS Team, W. Kasparek, and ECRH-Group, Phys. Rev. Lett. **90**, 075003 (2003).

[6] H. P. Laqua, H. Maassberg, F. Volpe, W7-AS Team, and ECRH-Group, Nucl. Fusion **43**, 1324 (2003), http://stacks.iop.org/NF/43/1324.

[7] P. McNeely, M. Barlak, J. Baldzuhn, S. Bozhenkov, M. Drevlak, G. Gawlik, B. Heinemann, D. Holtum, J. Jagielski, R. Kairys, R. Nocentini, R. Riedl, P. Rong, N. Rust, R. Schroeder, E. Speth, A. Stäbler, A. Turos, and R. Wolf, Fusion Eng. & Design **88**, 1034 (2013), Proceedings of the 27th Symposium on Fusion Technology (SOFT-27), Liège, Belgium, September 24–28, 2012.

[8] J. Ongena, A. Messiaen, D. van Eester, B. Schweer, P. Dumortier, F. Durodie, Y. O. Kazakov, F. Louche, M. Vervier, R. Koch, A. Krivska, A. Lyssovian, M. van Schoor, T. Wauters, V. Borsuk, O. Neubauer, O. Schmitz, G. Offermans, Y. Altenburg, C. Baylard, D. Birus, S. Bozhenkov, D. A. Hartmann, J. P. Kallmeyer, S. Renard, R. C. Wolf, and T. Fülöp, **21**, 061514 (2014).

[9] C. Beidler, G. Grieger, F. Herrnegger, E. Harmeyer, J. Kißlinger, W. Lotz, H. Maaßberg, P. Merkel, J. Nührenberg, F. Rau, J. Sapper, F. Sardei, R. Scardovelli, A. Schlüter, and H. Wobig, Fusion Technology **17**, 148 (1990).

[10] F. Warmer, C. D. Beidler, A. Dinklage, R. Wolf, and The W7-X Team, Plasma Phys. & Controlled Fusion **58**, 074006 (2016), Special Issue on the 20th International Stellarator-Heliotron Workshop, Greifswald, Germany, 5–9 October 2015.

[11] P. Grigull, K. McCormick, J. Baldzuhn, R. Burhenn, R. Brakel, H. Ehmler, Y. Feng, F. Gadelmeier, L. Giannone, D. Hartmann, D. Hildebrandt, M. Hirsch, R. Jaenicke, J. Kisslinger, J. Knauer, R. König, G. Kühner, H. Laqua, D. Naujoks, H. Niedermeyer, N. Ramasubramanian, N. Rust, F. Sardei, F. Wagner, A. Weller, U. Wenzel, and W7-AS Team, Plasma Phys. & Controlled Fusion **43**, 175 (2001).

[12] K. McCormick, P. Grigull, R. Burhenn, R. Brakel, H. Ehmler, Y. Feng, R. Fischer, F. Gadelmeier, L. Giannone, D. Hildebrandt, M. Hirsch, E. Holzhauer, R. Jaenicke, J. Kisslinger, T. Klinger, S. Klose, J. P. Knauer, R. König, G. Kühner, H. P. Laqua, D. Naujoks, H. Niedermeyer, E. Pasch, N. Ramasubramanian, N. Rust, F. Sardei, F. Wagner, A. Weller, U. Wenzel, and A. Werner, J. Nucl. Mat. **313-316**, 1131 (2003), Plasma-Surface Interactions in Controlled Fusion Devices 15, Gifu, Japan, 26–31 May 2002.

[13] Y. Feng, F. Sardei, P. Grigull, K. McCormick, J. Kißlinger, and D. Reiter, Nucl. Fusion **46**,

807 (2006), http://stacks.iop.org/NF/46/807.

[14] J. Boscary, A. Peacock, R. Stadler, B. Mendelevitch, H. Tittes, J. Tretter, M. Smirnow, and C. Li, **64**, 263 (2013), Proceedings of the Twentieth Topical Meeting on the Technology of Fusion Energy (TOFE-2012) (Part 1), Nashville, Tennessee, August 27–31, 2012.

[15] J. Geiger, C. D. Beidler, M. Drevlak, H. Maaßberg, C. Nührenberg, Y. Suzuki, and Y. Turkin, **50**, 770 (2010), Special Issue: Proceedings of 17th International Stellarator/Heliotron Workshop, October 12–16, 2009, Princeton Plasma Physics Laboratory (PPPL), Princeton, New Jersey, USA (Part II).

[16] A. Dinklage, C. D. Beidler, P. Helander, G. Fuchert, H. Maaßberg, K. Rahbarnia, T. Sunn Pedersen, Y. Turkin, R. C. Wolf, A. Alonso, T. Andreeva, B. Blackwell, S. Bozhenkov, B. Buttenschön, A. Czarnecka, F. Effenberg, Y. Feng, J. Geiger, M. Hirsch, U. Höfel, M. Jakubowski, T. Klinger, J. Knauer, G. Kocsis, A. Krämer-Flecken, M. Kubkowska, A. Langenberg, H. P. Laqua, N. Marushchenko, A. Mollén, U. Neuner, H. Niemann, E. Pasch, N. Pablant, L. Rudischhauser, H. M. Smith, O. Schmitz, T. Stange, T. Szepesi, G. Weir, T. Windisch, G. A. Wurden, D. Zhang, and W7-X Team, Nature Physics (2018), https://doi.org/10.1038/s41567-018-0141-9.

[17] Y. Turkin, H. Maassberg, C. D. Beidler, J. Geiger, and N. B. Marushchenko, **50**, 387 (2006), Selected Papers from Fifteenth International Stellarator Workshop (Part 2), Madrid, Spain, October 3–7, 2005.

[18] H. Hölbe, T. Sunn Pedersen, J. Geiger, S. Bozhenkov, R. König, Y. Feng, J. Lore, A. Lumsdaine, and Wendelstein 7-X Team, Nucl. Fusion **56**, 026015 (2016).

[19] A. Lumsdaine, J. Tipton, J. Lore, D. McGinnis, J. Canik, J. Harris, A. Peacock, J. Boscary, J. Tretter, and T. Andreeva, Fusion Eng. & Design **88**, 1773 (2013), Proceedings of the 27th Symposium on Fusion Technology (SOFT-27), Liège, Belgium, September 24–28, 2012.

[20] **51**, 99 (2011), erratum no. 2.

[21] J. Geiger, C. D. Beidler, Y. Feng, H. Maaßberg, N. B. Marushchenko, and Y. Turkin, Plasma Phys. & Controlled Fusion **57**, 014004 (2015).

[22] M. Zanini, H. P. Laqua, T. Stange, C. Brandt, M. Hirsch, U. Höfel, N. Marushchenko, U. Neuner, K. Rahbarnia, J. Schilling, H. Thomsen, R. C. Wolf, and W7-X Team, in *EPJ Web Conf.* (2019) p. 02013, Proceedings of the 20th Joint Workshop on Electron Cyclotron Emission (ECE) and Electron Cyclotron Resonance Heating (ECRH) (EC-20), Greifswald, Germany, 14–17 May

2018, https://doi.org/10.1051/epjconf/201920302013.

[23] M. Murakami, B. A. Carreras, L. R. Baylor, G. L. Bell, T. S. Bigelow, A. C. England, J. C. Glowienka, H. C. Howe, T. C. Jernigan, D. K. Lee, V. E. Lynch, C. H. Ma, D. A. Rasmussen, J. S. Tolliver, M. R. Wade, J. B. Wilgen, and W. R. Wing, Phys. Rev. Lett. **66**, 707 (1991).

[24] D. López-Bruna, J. A. Romero, R. Jiménez-Gómez, M. A. Pedrosa, M. Ochando, T. Estrada, A. López-Fraguas, F. Medina, J. Herranz, T. Kalhoff, E. Ascasíbar, A. de la Peña, and F. Lapayese, Nucl. Fusion **49**, 085016 (2009).

[25] H. Hölbe, *Control of the magnetic topology and plasma exhaust in the edge region of Wendelstein 7-X: A numerical study*, Ph.D. thesis, Ernst-Moritz-Arndt-Universität Greifswald (2015), https://d-nb.info/1080570160/34.

[26] J. D. Lore, M. Cianciosa, H. Frerichs, J. Geiger, H. Hoelbe, J. Boscary, and W7-X Team, IEEE Trans. Plasma Sci. **46**, 1387 (2018), Special Issue on Selected Papers from 27th Symposium on Fusion Engineering (SOFE), Princeton, NJ, 2017.

[27] J. D. Lore, T. Andreeva, J. Boscary, S. Bozhenkov, J. Geiger, J. H. Harris, H. Hoelbe, A. Lumsdaine, D. McGinnis, A. Peacock, and J. Tipton, IEEE Trans. Plasma Sci. **42**, 539 (2014).

[28] S. P. Hirshman and W. I. van Rij, Comp. Phys. Comm. **43**, 143 (1986).

[29] M. Drevlak, D. Monticello, and A. Reiman, Nucl. Fusion **45**, 731 (2005).

[30] W. I. van Rij and S. P. Hirshman, Phys. Fluids B: Plasma Phys. **1**, 563 (1989).

[31] Y. Turkin, C. D. Beidler, H. Maaßberg, S. Murakami, V. Tribaldos, and A. Wakasa, **18**, 022505 (2011).

[32] S. A. Bozhenkov, J. Geiger, M. Grahl, J. Kißlinger, A. Werner, and R. C. Wolf, Fusion Eng. & Design **88**, 2997 (2013).

[33] V. D. Shafranov and L. E. Zakharov, Nucl. Fusion **12**, 599 (1972).

[34] J. D. Hanson, Plasma Phys. & Controlled Fusion **57**, 115006 (2015).

[35] S. P. Hirshman, K. C. Shaing, W. I. van Rij, C. O. Beasley Jr., and E. C. Crume Jr., Phys. Fluids **29**, 2951 (1986).

[36] C. D. Beidler, K. Allmaier, M. Y. Isaev, S. V. Kasilov, W. Kernbichler, G. O. Leitold, H. Maaßberg, D. R. Mikkelsen, S. Murakami, M. Schmidt, D. A. Spong, V. Tribaldos, and A. Wakasa, Nucl. Fusion **51**, 076001 (2011).

[37] H. Maaßberg, C. D. Beidler, and Y. Turkin, **16**, 072504 (2009).

[38] M. Hirsch, J. Baldzuhn, C. Beidler, R. Brakel, R. Burhenn, A. Dinklage, H. Ehmler, M. Endler,

V. Erckmann, Y. Feng, J. Geiger, L. Giannone, G. Grieger, P. Grigull, H.-J. Hartfuß, D. Hartmann, R. Jaenicke, R. König, H. P. Laqua, H. Maaßberg, K. McCormick, F. Sardei, E. Speth, U. Stroth, F. Wagner, A. Weller, A. Werner, H. Wobig, S. Zoletnik, and W7-AS Team, Plasma Phys. & Controlled Fusion **50**, 053001 (2008).

[39] N. B. Marushchenko, Y. Turkin, and H. Maassberg, Comp. Phys. Comm. **185**, 165 (2014).

[40] P. Sinha, H. Hölbe, T. S. Pedersen, S. Bozhenkov, and W7-X Team, Nucl. Fusion **58**, 016027 (2018).

[41] D. Böckenhoff, M. Blatzheim, and W7-X Team, "Application of improved analysis of convective heat loads on plasma facing components to Wendelstein 7-X," (2019), Nucl. Fusion, in press, https://doi.org/10.1088/1741-4326/ab201e.

[42] R. Brakel, M. Köppen, A. Peacock, A. Werner, and M. Jakubowski, *Specification of Design Loads for In-vessel Components of W7-X*, Tech. Rep. (Max-Planck-Institut für Plasmaphysik, Greifswald, 2011) W7-X report no. 1-AC-S0005.0.

[43] G. Fuchert, K. J. Brunner, K. Rahbarnia, T. Stange, D. Zhang, J. Baldzuhn, S. A. Bozhenkov, C. D. Beidler, M. N. A. Beurskens, S. Brezinsek, R. Burhenn, H. Damm, A. Dinklage, Y. Feng, M. Hirsch, Y. Kazakov, J. Knauer, A. Langenberg, H. P. Laqua, S. Lazerson, N. A. Pablant, E. Pasch, T. Sunn Pedersen, E. R. Scott, F. Warmer, V. R. Winters, R. C. Wolf, and W7-X Team, in *Proceedings of the 27th IAEA Fusion Energy Conference, 22–27 October 2018, Gandhinagar, India* (IAEA, Vienna, 2019) pp. 286–291, paper IAEA-EX/3-5, https://conferences.iaea.org/indico/event/151/papers/5833/files/4764-iaea_template_fuchert.pdf, submitted to Nucl. Fusion.

[44] P. C. Liewer, Nucl. Fusion **25**, 543 (1985).

[45] H. Maaßberg, C. D. Beidler, U. Gasparino, M. Romé, and W7-AS Team, **7**, 295 (2000).

[46] Y. Suzuki, J. Geiger, M. Drevlak, and J. Nührenberg, in *33rd EPS Conference on Plasma Physics (Rome), 19 - 23 June 2006*, Europhysics Conference Abstracts, Vol. 30I, edited by F. De Marco and G. Vlad (European Physical Society, 2006) paper P-2.119, http://epsppd.epfl.ch/Roma/pdf/P2_119.pdf.

[47] Y. Narushima, S. Sakakibara, Y. Suzuki, K. Y. Watanabe, S. Ohdachi, Y. Takemura, M. Yoshinuma, K. Ida, F. Castejón, D. López-Bruna, C. C. Henga, M. Kobayashi, H. Tanaka, T. Akiyama, N. Ohno, and LHD Experimental Group, Nucl. Fusion **57**, 076024 (2017), https://doi.org/10.1088/1741-4326/aa6dce.